

# 6

---

## *Edge magnetisms and its application in two-dimensional atom-thin layers: Nanomeshes on graphene and black phosphorus*

---

Junji Haruyama\*

Faculty of Science and Engineering, Aoyama Gakuin University, 5-10-1 Fuchinobe, Sagamihara, Kanagawa 252-5258, Japan

\*Corresponding author

### **Outline:**

Introduction.....	119
Edge magnetisms in graphene nanomesh.....	119
Edge magnetisms in few-layer black phosphorus nanomesh.....	126
Tunnel magnetoresistance junctions created by ferromagnetic graphene nanomesh electrode...	135
Conclusion.....	140
References.....	141

## Introduction

The science and technology of 2D atom-thin layers have attracted considerable attention since the first fabrication of graphene, 2D carbon mono-atomic layer, by mechanical exfoliation of graphite via Scotch tapes. Among variety of phenomena observed in 2D atom-thin layers, magnetism arising from edge has attracted significant attention. Importantly, the edge magnetisms allow creation of magnetic and spintronic devices without using rare-(earth) magnetic elements. In this chapter, first, edge magnetisms observed in graphene nanomesh (GNM) will be presented. The zigzag-type atomic structure of graphene edges leads to spin polarization and subsequently appearance of flat-band FM from theoretical viewpoints. From experimental respect, flat-band FM has been realized based on the fabrication of zigzag-edged hydrogen (H)-terminated GNMs (H-GNMs) consisting of a honeycomb-like array of hexagonal nano-pores, fabricated using a non-lithographic method, resulting in the low-disordered and low-contaminated pore edges. Because a GNM corresponds to a large ensemble of zigzag-edged graphene nanoribbons (GNRs; 1D strip lines of graphene), it is effective to detect small magnetic signals arising from the pore edge spins.

Nevertheless, the observed magnetization values of the H-GNMs so far have been as small as  $\sim 10^{-6}$  emu/area except for some specific case using a HSQ resist treatment and are also far too small to allow envisioning practical applications. So, the experimental observation of room-temperature large edge FM in oxygen-terminated few-layer black phosphorus nanomesh (BPNM) will be presented in the second section. Mono- or few-layer BP has appeared as a 2D semiconductor with a substantial energy band gap connecting those of graphene and the transition metal dichalcogenides. The values of the observed robust edge FM per single pore are  $\sim 100$  times larger than that reported for H-GNMs, whereas the FM disappears in H-BPNMs. This is in highly contradiction to the case of GNMs and extremely interesting. The ferromagnetic coupling of the edge P atom with O atom and the strong spin localization of edge valence band can be the origins as well as the uniform oxidation of the pore edges and the interlayer edge interaction.

In the third section, realization of TMR junctions will be presented using the above mentioned ferromagnetic GNMs (FGNMs) as an electrode. Observation of TMR behaviors on the junction of cobalt/SiO<sub>2</sub>/FGNM electrode is shown, serving as a prototype structure for future rare-metal free TMR devices using magnetic graphene electrodes. Gradual change in TMR ratios is observed across zero-magnetic field, arising from specified alignment between pore-edge- and cobalt-spins. The TMR ratios can be controlled by applying back-gate voltage and by modulating interpore distance. Annealing the SiO<sub>2</sub>/FGNM junction also drastically enhances TMR ratios up to  $\sim 100\%$ . This paves the way for realizing high-efficiency 2D flexible magnetic and spintronic devices without the use of rare magnetic elements as atomic layers. These are highly important for next-generation magnetic and spintronic devices, which overcome the threat of lack of material resource.

## Edge magnetisms in graphene nanomesh

Carbon-based  $sp^x$ -orbital systems lead to rise of spin polarization (flat-band FM) based on strongly localized electrons at edges [1-7]. In particular, a specified atomic structure, the so-called zigzag type, at graphene edges has attracted large attention from the following two theoretical considerations [1-6, 10-22, 28-37].

One is the theory for GNR with two edges on its both sides along longitudinal direction. When the perfect edge-atomic structures without any defects are allowed, zigzag edge produces flat energy

band, resulting in an infinite effective mass of electrons and hence those strong localization. The localization yields extremely high density of electronic states (i.e., edge states), which induces strong spin interaction and subsequently appearance of spontaneous spin polarization. Two edges of a GNR allow that the these electron spins localizing at zigzag edges [1,10] are stabilized toward polarization (i.e., (anti) FM) due to the exchange interaction between the two edges, which produces a maximum spin ordering in these orbital, in a GNR [1-7], GNMs (see Fig. 6.1) [13,29], and graphene nanoflakes [14]. It is similar to the case of Hund's rule for atoms. Moreover, spin configuration is highly sensitive to kinds and number of foreign atoms (e.g., H and O), which terminated angling bonds of zigzag edges [3,31].

The other is the so-called Lieb's theorem [38], which assumes presence of low-concentration of defects in ensemble of carbon atoms (e.g. graphene flakes) resulting in appearance of net magnetism. It predicts the emergence of FM by an increase in the difference between the number of removed A and B sites ( $\Delta_{AB}$ ) of the graphene bipartite lattice (i.e., defects) at zigzag edges [14, 29, 31]. The magnitude of FMs increases with increasing values of  $\Delta_{AB}$ .

These two models are in contradiction from viewpoint of presence of the defects, while they provide very interesting spin configuration and certainly predict emergence of the spin polarization in all-carbon materials.

Almost no works, however, experimentally reported on observation of the edge magnetisms derived from graphene zigzag edges. One reason is because the edge-related phenomena are easily destroyed by presence of a large amount of disorder (damage, defects) and contamination introduced during fabrication process (e.g., by lithographic methods). Therefore, the following two original non-lithographic fabrication methods of graphene edges have been developed; (1) GNRs derived from unzipping of carbon nanotubes combined with air blow and three-step annealing [17] and (2) GNMs fabricated by etching graphene using nano-porous alumina template (NPAT) as masks [33]. In the present section, observation of the edge magnetisms in (2), GNMs, is reviewed [34-37].

### ***Non-lithographic fabrication of GNMs with zigzag pore edges***

The NPAT is easily fabricated through self-organization by anodic oxidation of pure (99.99%) aluminum substrate. It provides exceptionally high-regular array of hexagonal nano pores like a honeycomb (Fig. 6.1(a)). GNMs, which have honeycomb-like array of hexagonal nanopores (Figs. 6.1(b) and 6.1(e)), were fabricated on a large ensemble of mechanically exfoliated graphenes (or graphenes CVD-synthesized on SiC substrate) by using this NPAT [23] as an etching mask (Fig. 6.1(c)), following our previous nonlithographic method [33,42]. The graphene was carefully etched by optimized low-power Ar gas (e.g., 200–600 V for 10 – 40 min) so as to avoid giving damages to pore edges (Fig. 6.1(d)) and the honeycomb like NM of the NPAT (Fig. 6.1(a)) was transferred to graphene (Fig. 6.1(b)). Then, the NPAT was carefully detached from surface of the GNM by either mechanically (i.e., by pin set) or chemically (i.e., resolving the NPAT by chemical solutions).

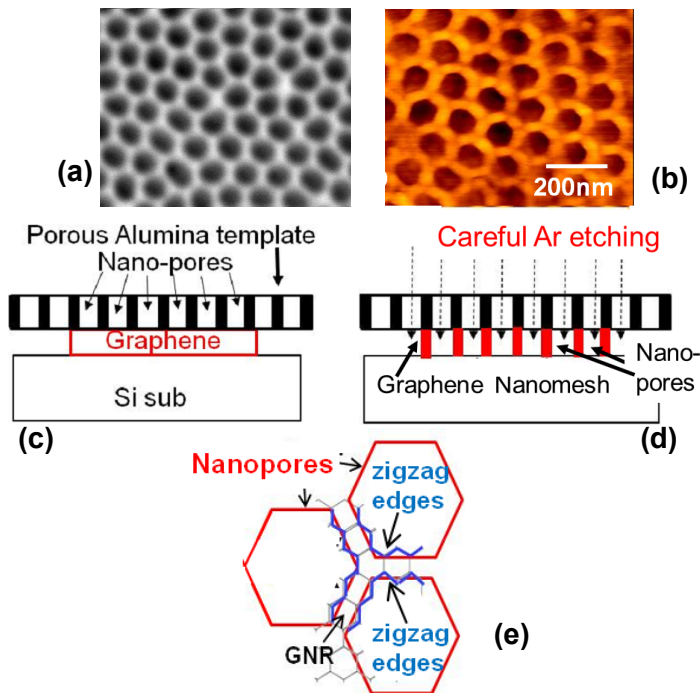


**FIGURE 6.1**

(a) SEM top view of a nano-porous alumina template (NPAT), which shows honeycomb-like array of hexagonal nano-pores. (b) AFM image of a GNM transferred from (a) following methods (c) and (d), with mean diameter  $\phi \sim 80$  nm and mean inter-pore distance  $W \sim 20$  nm. (c)(d) Schematic cross sectional views of non-lithographic fabrication process of a GNM. (c) NPAT was placed on graphene as an etching mask. (d) The graphene is carefully etched by Ar gas, resulting in formation of a GNM with low-damages and low-contamination pore edges. (e) Schematic view of a GNM with the zigzag-type pore-edge. Interpore regions can correspond to GNRs. Actual interpore regions include a larger number of hexagonal carbon unit cells per inter-pore region with length  $\sim 40$  nm and  $W \sim 20$  nm. This GNM structure brings at least three large advantages as mentioned in text. [34,35]

All the GNMs fabricated following these processes were annealed at a critical temperature ( $T_c$ ) of  $800^\circ\text{C}$  in high vacuum ( $10^{-6}$  Torr) for 0.5 – 3 days with keeping pumping of gas and, then, in  $\text{H}_2$  gas by the field-emission-type radical CVD system under pressure  $> 1\text{MPa}$  at least for 3 hours at for all the measurements. The first annealing allows deoxidization of the pore edges with recovering all damages and defects and essential to form zigzag pore edges by edge atomic reconstruction, while the second annealing is important for termination of the edge dangling bonds at the pore edges by H atoms. For O-termination, the GNM was annealed at  $800^\circ\text{C}$  in oxygen atmosphere for 1 hour right after the  $T_c$  annealing as mentioned above. DC magnetization measurements were carried out right after the annealing by a superconducting quantum interference device (SQUID; Quantum Design).

At least the three significant advantages are brought by this method as follows. (1) It gives much low-concentration of defects and low-contamination to the nanopore edges of GNMs due to the non-lithographic method. (2) The honeycomb-like array of hexagonal nanopores leads to the formation of a large amount of GNRs and pore edges with sufficient lengths (e.g., 40 nm in the

present case), because one hexagonal nanopore can have six edges and the inter-pore regions can correspond to GNRs (Fig. 6.1(e)). In the actual GNM, it is speculated that mixture of zigzag and armchair edges exists in one inter-pore GNR (one pore edge), as reported by previous STM observation [9]. Even if so, a large number of GNRs in the present GNMs yield a large amount of the assembled zigzag-edge GNRs. This is extremely effective to sense small magnetic and electric signals arising from the pore edges. (3) When one would align the atomic structure of one pore edge to zigzag, the other five pore edges can automatically become zigzag structure from a topological reason. To date, this has not been realized and zigzag pore edges have been formed only via the  $T_c$  annealing, unlike Ref. [22].

No direct observation for presence of zigzag-type pore edges is presented in this chapter. In Ref. [33], however, presence of zigzag atomic structure at the pore edges has been confirmed by observation of the highly suppressed ratios of D/G band peak heights ( $< 0.2$ ) in Raman spectra. It was realized via reconstruction of edge atomic structure to zigzag type by the  $T_c$  annealing. Indeed, two groups reported on similar correlation in intentionally fabricated zigzag-edged hexagonal nanopores [20] and also graphene flakes [30]. Although the low D/G band peak ratios can be conventionally evidence just for low defects in samples, it can turn out the zigzag pore edges in the present case in which one dimensionality of the GNR edges is dominant [30].

As mentioned above, zigzag-type pore edge cannot be intentionally formed (e.g., despite the advantage (3) mentioned above). Refs. [15] and [16], however, suggested that zigzag edge is the most stable from chemical and thermal viewpoints and that all arm chair-based edges are finally reconstructed to zigzag after STM Joule heating for long edges of overlapped graphenes [15] and electron beam (EB) irradiation to pore edges [16]. This stability may be simply understood by difference in the number of carbon atoms bonded to two neighboring carbon atoms (dangling bonds) for zigzag edge (i.e., one such atom) and arm chair edges (two such atoms) [16]. After removal of such atoms, arm chair edge requires energy two-times larger than zigzag in order to repair the removed atoms and, thus, becomes unstable. In our system, we carried out high-temperature annealing for narrow ( $W \sim 20$  nm) GNRs (i.e., narrow inter-pore spacing). It must bring the energy similar to those in Refs. [15, 16] and cause the reconstruction of pore edge atomic structures to zigzag.

### ***Magnetism depending on pore edge termination by different foreign atoms***

Observation of magnetizations measured for GNMs with different ad atoms terminating pore edges are shown in Fig. 6.2(a). Ferromagnetic-hysteresis loop with large amplitude is clearly observed only in H-GNM in Figs. 6.2(a) and 6.2(d), which showed the low D/G peak ratio values ( $< 0.2$ ). In addition to this sample, other three samples with the low D/G peak heights in Raman spectra exhibited similar FM. In contrast, O-GNMs exhibit a diamagnetism-like weak hysteresis loop (Figs. 6.2(b) and 6.2(e)). This is consistent with Ref. [6], which reported that the formation of a spin-paired C=O chemical bond drastically reduces the local atomic magnetic moment of carbon at the zigzag edge of GNRs and suppresses the emergence of FM.

Bulk graphenes without any pores and those assembled with NPATs show mostly no such features even after  $H_2$  annealing (Figs. 6.2(c) and 6.2(f)), implying no contribution of parasitic factors (e.g., defects, impurities) of bulk graphenes. Moreover, presence of less damages or impurities is reconfirmed in the most of bulk-graphene regions, because mechanically exfoliated bulk graphenes show an extremely low D/G peak heights ( $\ll 0.1$ ) and a high 2D peak intensity in the Raman spectrum. These results strongly suggest that the observed FM is associated with polarized spins localizing at the H-terminated zigzag-pore edges. It should be noticed that the FM observed at 2 K

remains unchanged even at room temperature with a larger magnitude of the hysteresis loops (Fig. 6.2(d)).

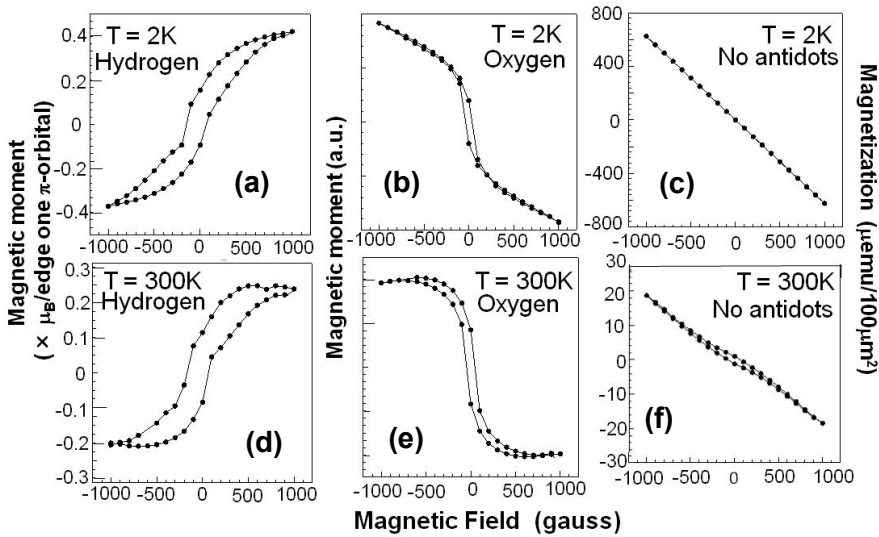


**FIGURE 6.2**

Magnetization of monolayer GNMs with  $\phi \sim 80$  nm and  $W \sim 20$  nm for termination by different atoms. **(a)(d)** H-termination; **(b)(e)** O-termination; **(c)(f)** bulk graphene without pore arrays. Magnetic fields were applied perpendicular to GNMs. The vertical axis in (a) and (d) denote magnetic moment per localized-edge  $\pi$  orbital, assuming mono-hydrogenation of individual edge carbon atoms [34,35]

Figure 6.3 shows magnetization curves as a function of the inter-pore spacing (i.e., corresponding to the width of the GNR,  $W$ ; Fig. 6.1(e)). It is found that the magnitude of hysteresis loop decreases with increasing  $W$ . In particular, it is revealed that the residual magnetization is inversely proportional to  $W$  value (inset of Fig. 6.3(c)). This result is qualitatively consistent with theories for GNR model according to which the edge spin stability and ordering of a zigzag-edge GNR are determined by the exchange interaction between the two edges leading to vanishing of ferromagnetic edge spin ordering with increase of  $W$  [2,5]. Such a correlation cannot be understood by the FM originating from the defects located only at pore edges or in the bulk graphene between pores. In the former case, FM amplitude should be mostly independent of  $W$ , because defects locate only at pore edges. In the latter, FM amplitude should increase with an increase of  $W$ , because density of defects increases. Consequently, we conclude that the observed FM is not due to parasitic origins (e.g., defects, impurities) but can be truly attributed to  $H$ -terminated zigzag pore edges.

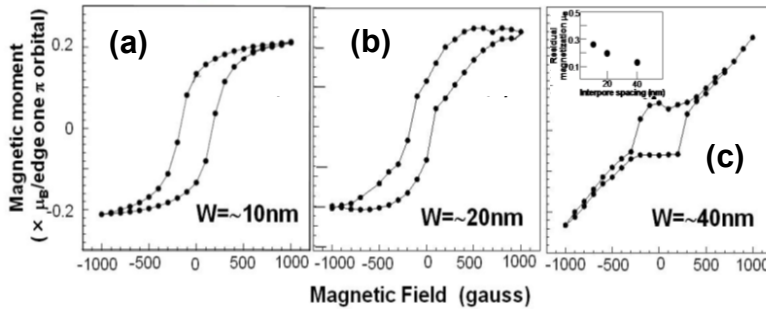


**FIGURE 6.3**

The observed FM as a function of the mean inter-pore spacing  $W$  at  $T = 300$  K. Mean pore diameter ( $\phi \sim 80$  nm) was kept through all samples. For Figs. 6.3 (a) – (c), difference in magnetic moment between upper and lower curves of hysteresis loop at  $H = 0$  (residual magnetization  $B_r \times 2$ ) is  $\sim 0.28 \mu_B$ ,  $\sim 0.2 \mu_B$ ,  $\sim 0.12 \mu_B$  and the loop width at zero magnetic moment (coercivity  $H_c \times 2$ ) is  $\sim 400$  gauss,  $\sim 260$  gauss,  $\sim 500$  gauss, respectively. **Inset of (c)**;  $B_r$  at 300 K as a function of  $W$ . [34,35]

This is also consistent with observation by magnetic force microscope (MFM) (Fig. 6.4). It obviously exhibits presence of high density of polarized spins at the inter-pore GNR regions and also edge polarized spins at some pore edges. Because non-ferromagnetic samples shows no such features, the observed FM is attributed to these polarized spins. Approximately 50% of the samples, which include samples showing the low D/G peak heights, have shown FM.

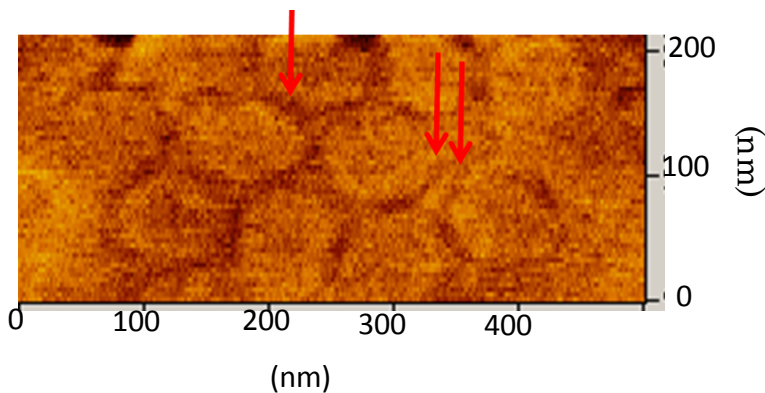


**FIGURE 6.4**

Magnetic force microscope images of an H-terminated ferromagnetic GNM on SiC substrate. CoPtCr-coated Si probe was used for the measurements with a tapping mode. The inter-pore regions, which correspond to GNRs and exhibit darker color, imply high density of polarized spins. They directly suggest that the observed FM originates from the GNRs. In particular, two arrow-parts evidently imply presence of edge polarized spins. [34,35]

#### **Defect-dependent two theoretical models: GNR model and Lieb's theorem**

Defect-dependent two theoretical calculations quantitatively support the interpretation mentioned above. First, the GNR model, which assumes pure zigzag pore edges (i.e., without any defects) at all regions, allows estimating the magnetic moment of edge carbon atoms that contributes to the FM observed in Fig. 6.2. Assuming that only edge dangling bonds have localized spin moments, the

magnetic moment per edged angling bond prior to  $H$  termination is estimated to be  $(1.2 \times 10^{-23})/(\mu_B = 9.3 \times 10^{-24}) \sim 1.3 \mu_B$ , where  $\mu_B$  is the Bohr magneton, from the following.

The magnetic moment per edged angling bond prior to  $H$  termination is estimated according to the following steps; (1) the total area of assembled bulk graphenes used for the pore array formation is  $\sim 4 \text{ cm}^2$ . (2) The area of one hexagonal unit cell with a pore is  $S = 6(3^{-1/2}/2)(a/2)^2 \sim 4300 \text{ nm}^2$ , where  $a = [80 \text{ nm (pore diameter)} + 20 \text{ nm (interpore spacing)}]$ . (3) Thus, the total number of pores is  $(4 \text{ cm}^2)/(4300 \text{ nm}^2) \sim 10^{11} [(1)/(2)]$ . (4) The total number of dangling bonds perhexagonal pore is  $(40 \text{ nm})/(0.142 \text{ nm} \times 3^{1/2}) \times 6 = 166 \times 6 \sim 1000$ . (5) The total number of edge dangling bonds of the GNM used for the SQUID measurement is  $10^{14} [(3) \times (4)]$ .

Therefore, using (5), the saturation magnetization per edge dangling bond is estimated to be  $1.2 \times 10^{-6} \text{ (emu)} \times 10^{-3}/10^{14} = 1.2 \times 10^{-23} \text{ (J/T)}$ . Thus, the magnetic moment per edge dangling bond is estimated to be  $(1.2 \times 10^{-23})/(\mu_B = 9.3 \times 10^{-24}) \sim 1.3 \mu_B$ , where  $\mu_B$  is the Bohr magneton. Conventionally, GNRs with no  $H$ -termination of dangling bonds should show anti-FM, theoretically. However, in the above estimation, the observed total magnetization was divided by estimated number of edge dangling bonds in the GNM, neglecting this theory.

Next, after  $H$  annealing at  $T_c$ , edge dangling bonds of a GNR are terminated by  $H$  atoms [3,5-7,9]. The following three types of  $H$  terminations are theoretically possible. (1) All edge dangling bonds are each terminated by one  $H$  atom on both-side zigzag edge. It provides a flat band for  $2\pi/3 \leq k \leq \pi$  in the Brillouin zone. Electrons are well localized at the edges. (2) All the edge dangling bonds of one side are each terminated by two  $H$  atoms (so that the edge carbon atom becomes tetrahedrally coordinated; a bearded edge), while the opposite-side dangling bonds are terminated by a single  $H$  atom. The GNR provides a flat band for  $0 \leq k \leq \pi$ , resulting in a completely localized "on-bonding state" around the Fermi level ( $E_F$ ). This leads to the spin polarization of all carbon atoms. (3) The double  $H$  atom termination of the zigzag-edge carbon atoms on both sides of a GNR provides a flat band for  $0 \leq k \leq 2\pi/3$  and creates a modified zigzag edge.

The type of edge  $H$ -termination could not be observed in the present experiment. However, our case should correspond to case (1) from the following reason. The mono- $H$  termination of the edge dangling bond decreases its magnetic moment to one  $\mu_B$ . The magnetic moment of one localized-edge  $\pi$  orbital is, therefore, estimated to be as large as  $(\sim 1.3\mu_B - 1\mu_B) = \sim 0.3\mu_B$ . This is in fairly good agreement with the theoretical contribution of the  $\pi$ -orbital state to the edge magnetic moment of  $\sim 0.3 \mu_B$  in a zigzag-edged GNR within the ferromagnetically ordered spin configuration [5].

As the other model, Lieb's model [29], which predicts appearance of net magnetization arising from small defects in sublattice of carbon hexagonal cell (i.e., missing A and B sites underlying bipartite lattice), is used. Even a small defect may still remain in actual pore edges. In order to elucidate the influence of such residual small-volume edge disorder on magnetism of GNM, Yang et al. performed systematic first-principles calculations of magnetic properties of quasi-GNR structures (Fig. 6.5(a), corresponding to the inter-pore region) based on Lieb's theorem [29], which introduces the slight disorder at upper edge. Interestingly, the ground state of quasi-GNR structure turned out to be ferromagnetic in Fig. 6.5(b). The calculated net magnetic moment follows Lieb's theorem with local moments up to  $0.2\mu_B/\text{edge atom}$  and depends on magnitude of the assumed edge disorder. These values agree fairly well with the value estimated from the GNR model

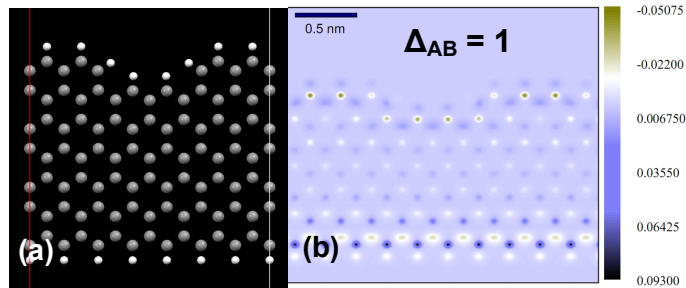


**FIGURE 6.5**

**(a)** Schematic view of structure of mono-hydrogen-terminated inter-pore GNR region, which introduces small curvature (defects) with  $\Delta_{AB}=1$  (i.e., the difference between the number of removed A and B sites of the graphene sublattices at zigzag edges) on the upper edge, used for first-principles calculations based on Lieb's theorem. The dark and white atoms are carbon and hydrogen, respectively. **(b)** Calculated spin-density distribution of quasi-GNR for (a). It reveals appearance of ferromagnetic spin configuration at the lower edge, which gives the edge magnetic moment of  $0.2\mu_B$ . [calculated by H. Yang and M. Chshiev ref. (34,35)]

Consequently, both models theoretically support that the observed FM can originate from mono-hydrogenated zigzag nanopore edges. In order to determine which models are more appropriate to the actual structures, direct observation of the pore edge atomic structures and number of the H atoms are indispensable. If GNR model would be relevant, presence of no defects at the pore edges is assumed. This may be realistic, because there are so many carbon atoms on one pore's edges and also so many nano pores in one GNM as mentioned above. In contrast, if Lieb's theorem would be applicable, small amount of defects should exist at the pore edges. However, following the above calculation, ferromagnetic spin alignment does not appear at the edge including defects in this case. This seems to be in poor agreement with the results of MFM observation mentioned above. Further experiments and comparison with theories are, therefore, indispensable.

The edge states of FGNMs have been also confirmed by observation using ionic liquid gate [36]. Even much higher magnetization values in mono-H-terminated FGNMs have been realized by using specific technique (i.e., by using an electron beam (EB) resist treatment with EB irradiation) [37]. Further advancement must realize rare-magnetic element free magnets and spin devices. Recently, even spin Hall effect and topological insulating state have been predicted and realized in graphene [25-27].

## Edge magnetisms in few-layer black phosphorus

Flat-band FM in H-GNMs has been explained in section 1. Nevertheless, the observed magnetization values so far have been as small as  $\sim 10^{-6}$  emu/area, except for some specific case using the electron beam resist treatment method [37]. The value is insufficient for actual device application.

On the other hand, mono- or few-layer BP have recently appeared as a 2D semiconductor with a substantial energy band gap [39,40]. BP has a puckered honeycomb lattice, easily oxidized under air atmosphere exposure, with an in-plane anisotropic atomic structure (i.e., zigzag within monolayer and buckling armchair formed over two layers; Fig. 6.6(a)) [39-50]. Regarding those magnetisms, only theoretical works have been reported up to now [43,44,47]. In particular, spin polarization arising from edge dangling bonds has been predicted in pristine zigzag-edged phosphorene

nanoribbons (ZPNRs), when non-fully relaxed structure was assumed in order to avoid Peierls transition [43]. This predicted local edge magnetic moments  $M_L$  of  $0.27 \mu_B$  for the O atom,  $0.39 \mu_B$  for the edge P atom, and  $0.13 \mu_B$  for its nearest neighbor, respectively, in O-terminated case. O-saturated zigzag PNRs show this edge FM due to the spins of unsaturated bonds in weak P–O bonds along the  $p_z$  orbitals in the NR plane, whereas H-terminated zigzag PNRs show no edge FM. This behavior highly contrasts with that of GNMs, in which H-terminated zigzag edges yielded flat-band FM while O-terminated edges exhibited diamagnetism, described in section 1. Moreover, even stronger and highly stable edge anti-FM (AFM) has been predicted in ZPNRs due to the electronic instability induced by the half-filled 1D bands [47]. The half-filled 1D bands crossed the Fermi level at around  $\pi/2a$  for ZPNRs, showing emergence of no Peierls transition. This with edge-AFM ordering reported  $0.155 \mu_B$  for the edge P. However, no experiments have been performed to confirm these intriguing magnetic properties of BP edges. In this section, a large edge magnetism observed in few-layer BPNMs fabricated the same non-lithographic method as those for FGNMs is described [65]. The observed magnetization values are almost 100 times larger than that in FGNMs.

### **Sample fabrication and characterization**

In the present experiments, flakes of few-layered BPs were mechanically exfoliated from bulk BP (Smart Element Co.) using the Scotch tape method and observed via optical microscope (Fig. 6.6(c)) and atomic force microscope (Fig. 6.6(d)). Following application of a non-lithographic method used for GNMs (i.e. using nano-porous alumina template as an etching mask), few-layer BPNMs were fabricated (Figs. 6.6(b) and 6.6(c)). Interpore regions correspond to BPNRs, but only two edges of each hexagonal pore can be simultaneously perfect zigzag shaped because of the topological reason that the inner angle of the puckered honeycomb lattice  $\sim 98.15^\circ$  (Fig. 6.6(b)) cannot be aligned to the inner angle of the hexagonal pore of  $120^\circ$ . This is different from the case of GNM.

After the formation of nanopore array, the BPNMs were annealed at a critical temperature ( $T_c$ ) of  $300^\circ\text{C}$  in a high vacuum ( $\sim 10^{-6}$  torr) in order to form the zigzag pore edges by the edge atomic reconstruction similar to the case of zigzag-GNMs, because BPNMs consisting of ensemble of the narrow NRs disappear due to atom diffusion by the annealing at  $T > T_c$ .

Absence of substantial background magnetic impurities and magnetic contamination (e.g., Ni, Fe, Co) has been carefully confirmed by the following methods; (1) XPS measurement of three BPNMs (Fig. 6.6(f)), (2) Observation of magnetization of two-type few-layer bulk BP flakes (i.e., without pores) [Type A; explained for main panel of Fig. 6.7(b), which has taken all the same fabrication process as those for BPNM (Fig. 6.7(a)-sample) except for forming pores and Type B; for inset of Fig. 6.7(b), in which Ar gas etching process was carried out without using porous alumina template mask by the same condition as that for pore forming of BPNM), (3) Investigation of dependence of magnetisms on foreign atoms terminating the pore edges of BPNMs. (4) Careful check of absence of magnetic materials and instruments during for fabrication.

For (1), Fig. 6.6 factually exhibits no peaks of typical magnetic orbitals. For (2), absence of magnetic hysteresis loops in both types is shown in Fig. 6.7(b) as below. For (3), significant difference for H and O terminations is shown in Figs. 6.7(a) and 6.7(d) as below, compared with those of GNMs. If the observed magnetism originates from magnetic impurities introduced in the fabrication process being exactly the same for BPNM and GNM, such difference should not be observed, basically. For (4), the use of no magnetic staff has been much carefully confirmed [e.g., in bulk BPs used for mechanically exfoliation and scotch tapes, porous alumina templates using extremely pure Al substrate (99.99 %) for anodic oxidation and its oxidation process, Ar gas etching process for pore

formation, and also using plastic tweezers for any processes]. All of these results certainly turn out absence of any parasitic magnetic-background.

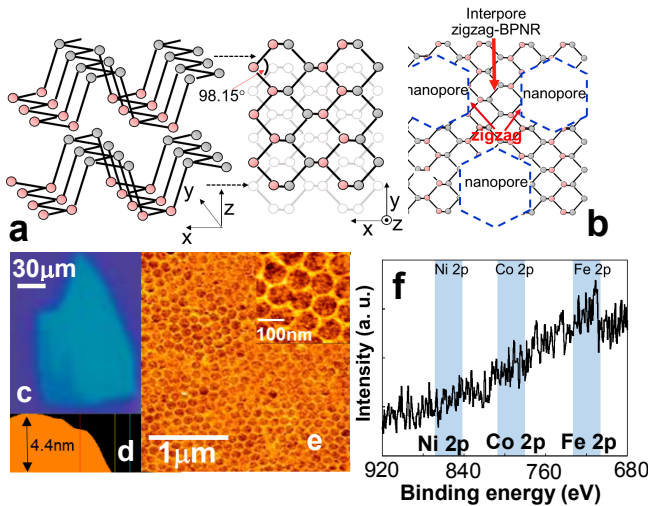


**FIGURE 6.6**

(a) Schematic cross-sectional and top views of a pucker honeycomb lattice of two-layer BP with AB stacking. Gray and red symbols P atoms locate within different height. Zigzag edge is within mono layer along y axis, while buckling arm chair edge is formed to z-axis direction along x axis. (b) Schematic top view of a BPNM, in which two pore edges are perfectly aligned to zigzag structure. In actual structure, pore size and interpore spacing are much larger and larger number of P atoms exists at the interpore BPNR regions. (c) Example of optical microscope image of a flake of few-layer BP mechanically exfoliated from bulk BP. (d) Cross-sectional image of (c) obtained using atomic-force microscope. One sample consists of main large flakes and other many small flakes with number of  $10\sim 10^2$ . Thickness and area of all flakes including small flakes have been measured so as to be  $0.1\sim 0.4\text{ cm}^2$  of the total area with similar thickness in one sample. (e) Atomic-force microscope top-view image of a BPNM with a large number ( $\sim 10^{12}$ ) of pores, which was fabricated via non-lithographic method in an extremely careful way (e.g., using plastic tweezers) to avoid incorporating magnetic impurities, defects, and contamination. **Inset:** Higher magnification image. (f) XPS spectra of a ferromagnetic BPNM. The binding energies have been calibrated at the Si 2p level in  $\text{SiO}_2$  (103.3 eV).  $2p_{3/2}$ -binding Energies are 853.8 eV for Ni in  $\text{NiO}_2$ , 780.4 eV for Co in  $\text{CoO}$ , and 710.9 eV Fe in  $\text{Fe}_2\text{O}_3$ . [65]

Subsequently, each BPNMs was placed in an air atmosphere at 300 K for 2 h, resulting in O-termination of pore edges (i.e., O-termination of the pore edges, because oxidized top layers serve as protection layers of underneath BP layers preventing their bulk oxidation). Immediately following this annealing process, magnetization was measured using superconducting quantum interference devices (Quantum Design Co.).

### **Magnetization measurements of various samples**

Figure 6.7(a) shows measurement results of the magnetization of the O-BPNM. Ferromagnetic (FMC)-hysteresis loops are observed with  $M_s \sim 10^{-4}\text{ emu}/\sim 0.4\text{ cm}^2$ . Order of this  $M_s$  is approximately 100 times smaller than those in H-terminated FGNMs (i.e.,  $M_s \sim 10^{-6}\text{ emu}$ ). Importantly, the hysteresis loop at  $T = 2\text{ K}$  approximately remains as it is even at  $T = 300\text{ K}$ . On the other hand, two-type few-layer bulk BP flakes without pores as mentioned above show no magnetization (main panel and inset of Fig. 6.7(b)). These important results indirectly reconfirm that the FM observed in

Fig. 6.7(a) originates solely from the formation of oxidized nano-pores. This has been confirmed at least in three samples.

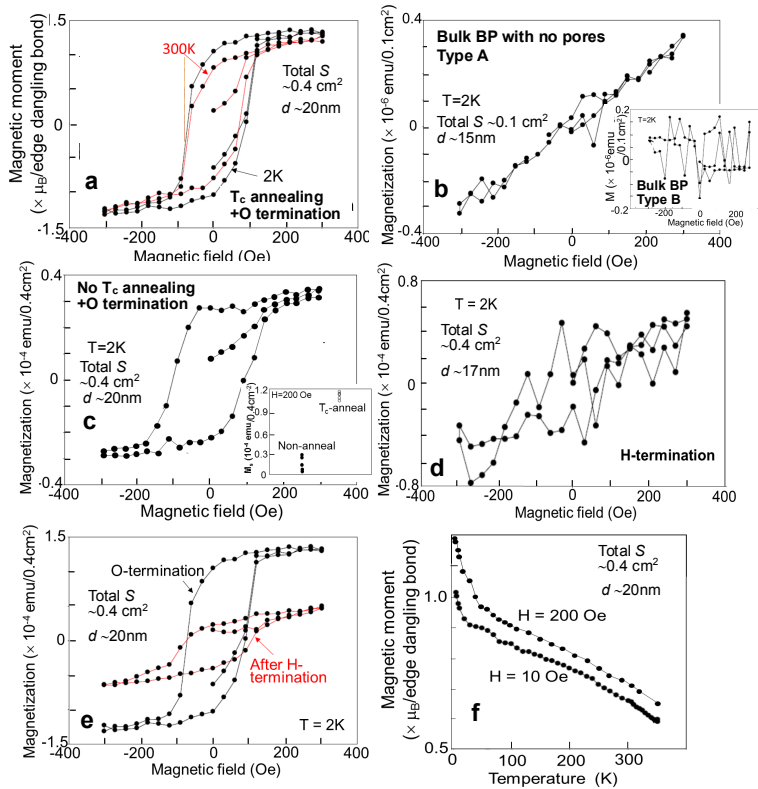
Since the oxidation of pore edges is easily obtained by exposing BPNM into air atmosphere, one can assume that all pore edges in a BPNM are O-terminated and can become magnetic. When it is assumed that atomic structure of all the pored edge is zigzag and fully O-terminated, the magnetic moment per edge dangling bond in hexagonal pores is estimated to be  $\sim 1.0 \mu_B$ , where  $\mu_B$  is the Bohr magneton. This value is in good agreement with calculation result of the magnetization value of edge P=O bond explained later in theoretical part. Accordingly, BP has a significant advantage in which O-terminate edge generate room-temperature magnetism, in contrast with the much smaller magnetism obtained by partially H-terminated edges in GNM.

Figure 6.7(c) reveals that the non-annealed BPNM demonstrates a FMC hysteresis loop with a  $M_s$  value  $\sim 4$  times less than those of the  $T_c$ -annealed samples (i.e., Fig. 6.7(a)). This result implies that annealing at the  $T_c$  is important for introducing large FM. Indeed, reproducibility of magnetism in non-annealed BPNMs is poor and some samples even show  $M_s$  values smaller than  $\sim 0.3 \times 10^{-4}$  emu/ $100 \mu\text{m}^2$  (inset of Fig. 6.7(c)). In the FMC-GNMs, the zigzag-type edge atomic structure is the most stable structure from both thermal and chemical perspectives, hence annealing at the  $T_c$  resulted in the formation of zigzag pore edges and the subsequent appearance of FM after H-termination. The occurrence of similar pore-edge atomic reconstruction to a zigzag is also expected for the pores of the present BPNMs (Fig. 6.6(b)) following annealing at the  $T_c$ , thus also leading to FM after O-termination (Fig. 6.7(a)). This can be confirmed by Raman spectroscopy in later part.

Figure 6.7(d) shows the magnetization curve for the BPNM obtained after annealing under an  $\text{H}_2$  atmosphere at  $300^\circ\text{C}$  for 2 h immediately after formation of the nanopores. In contrast to the O-BPNM, it can be seen that the H-BPNM barely exhibit a FMC-hysteresis loop and the magnetic signal is paramagnetic but noisy. Moreover, the  $M_s$  of an O-BPNM subsequently annealed under an  $\text{H}_2$  atmosphere at  $T_c \sim 300^\circ\text{C}$  for 5 h (Fig. 6.7(e)) is  $\sim 3$  times less than that of the original O-BPNMs (Fig. 6.7(a)).

The disappearance of FM in the H-BPNM is consistent with the theoretical prediction of the disappearance of FM in PNRs with H-terminated zigzag edges. In particular, the result in Fig. 6.7(e) suggests that O-termination of the zigzag pore edges is highly stable and cannot be entirely replaced by H-termination.

Temperature-dependence of  $M_s$  and magnetization close to residual magnetization ( $M_r$ ) are shown in Fig. 6.7(f). Both  $M$  values monotonically increase with decreasing temperature (e.g., from  $\sim 0.65 \times 10^{-4}$  emu/ $0.4 \text{ cm}^2$  (300K) to  $\sim 1.0 \times 10^{-4}$  emu/ $0.4 \text{ cm}^2$  (2K) for  $H = 10$  Oe and  $\sim 0.7$  (300K) to  $\sim 1.2$  (2K) for  $H = 200$  Oe). Hence, the difference of  $M_s$  and  $M_r$  values between 2K and 300K is evident. This result definitely supports the presence of the FMC hysteresis loops at 2K and 300K in our O-BPNMs. Curie temperatures of measured all FMC-BPNMs are above  $350^\circ\text{C}$ , which is the upper limit temperature of our SQUID.



**FIGURE 6.7**

(a, c-e), Magnetization curves for BPNMs with (a)  $T_c$  annealing and O-termination, (c) no  $T_c$  annealing and O-termination, (d) H-termination, (e) H-termination of the sample in (a). Y-axis of Figs. 6.7(a) and 6.7(f) has been normalized by number of O-terminated edge dangling bond of pores. **Inset of (c)**, Saturation magnetization ( $M_s$ ) of  $T_c$ - and no  $T_c$ -annealed BPNMs (each five samples) BPNMs at 2K. **(b)** Magnetization curve for Type-A few-layer bulk BP flake obtained through all the same fabrication process as those for (a)-sample except for the pore formation. **Inset of (b)**; Magnetization for Type-B bulk thick BP, in which Ar gas etching process was carried out without using porous alumina template mask by the same Ar gas condition as that for pore forming. For all samples, no background magnetism was subtracted except for (c), in which a diamagnetic background line was subtracted.  $S$  is the sample area including the total pore area. Results of Fig. 6.7(b) are independent of  $S$ . **(f)** Temperature dependence of magnetization values of a magnetic BPNM (i.e., with  $T_c$  annealing and O-termination) measured with decreasing temperatures. [65]

**Structure dependence of ferromagnetism of O-terminated BPNMs**

Figure 6.8 shows the  $M_r$  of FMC-BPNMs (O-BPNMs) as a function of the interpore distance ( $W$ ), which is identical to the width of a PNR, and  $M_s$  as a function of the thickness ( $d$ ) and sample area ( $S$ ). The  $M_r$  value seems to be not very sensitive to  $W$  (Fig. 6.8(a)). This is controversial when compared to flat band FM in GNMs, there the Coulomb exchange interaction between opposite edges strongly decreases with  $W$ , leading to a loss of the stability of the FMC spin ordering and hence a lower  $M_r$ . This is, however, consistent with previous theories of ZPNRs and with our theoretical prediction described below.

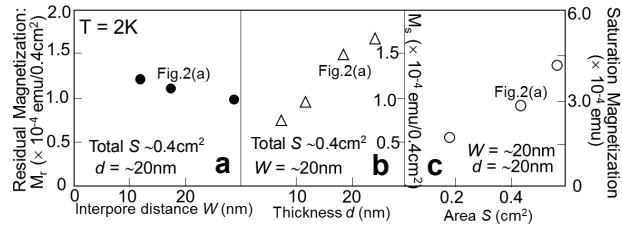


**FIGURE 6.8**

**(a)** Residual magnetization ( $M_r$ ) of FM BPNMs as a function of the interpore distance ( $W$ ) (i.e., width of the interpore PNR regions), and  $M_s$  as a function of the **(b)** thickness ( $d$ ) and **(c)** sample area ( $S$ ). Fig.6.7(a)- sample is noted on individual figures.  $W$  has been controlled by that in porous alumina template mask formed by changing temperature of anodic oxidation of Al substrate e.g., ( $0 \sim 10^\circ\text{C}$ ). In contrast, samples with different  $d$  and  $S$  have been selected from many random samples. [65]

On the other hand, the  $M_s$  values are linearly enhanced as  $d$  and  $S$  increases (Figs. 6.8(b) and 6.8(c)). In particular, the dependence on  $d$  suggests that  $M_s$  value of mono-layer BPNM becomes negligible. This is associated with strong interlayer interactions in AB stacking of BP (Fig. 6.6(a)), which favors the FMC spin configuration and analogous to graphene [14]. Our theoretical calculations for zigzag-PNR actually support this result and also indicate even much stronger interlayer interaction as explained in later part (Fig. 6.10(d)(e)). This interlayer spin interaction makes long-range spin ordering stable even at 300 K (Fig. 6.7(a)). The linear dependence on  $S$  (Fig. 6.8(c)) arises because the area of the O-terminated zigzag pore edges linearly increases with increasing  $S$ . This means that the fully O-terminated pores uniformly exist through all layers in individual samples. This implies that the O-termination of the pore edges of BPNMs can be easily realized only by exposing samples to air atmosphere and significantly contributes to the observed large-magnitude edge magnetisms.

As discussed above, annealing at  $T_c$  may cause the reconstruction of the pore-edge atomic structure, resulting in formation of zigzag pore edges and subsequent occurrence of FM after O-termination. Because the BPNM tends to disappear when annealing at  $T > 350^\circ\text{C}$ , the annealing temperature of  $300^\circ\text{C}$  is approximately the  $T_c$ , at which the reconstruction of pore-edge atomic structures occurs in the BPNMs. This  $T_c$  is much lower than  $\sim 800^\circ\text{C}$  for the FGNMs.

### **Raman spectroscopy: zigzag edge formation by reconstruction**

Evaluation of typical Raman spectra of BPNMs that did and did not exhibit FM evidently supports this argument (Fig. 6.9(a)). From Fig. 6.9(a), it is confirmed that the heights of the band peaks due to the phonons resulting from interlayer interactions ( $I_{Ag1}$ ) are nearly the same in the spectra of the two samples, while the intensity of the band attributed to the phonon from the Si substrate ( $I_{Si}$ ) is significantly larger in the non-FMC sample, leading to a low  $I_{Ag1}/I_{Si}$  value. We find that this tendency agrees with that confirmed for the bulk regions and edges of few-layer BP flakes (i.e., without nano-pores) of different  $d$  that were not annealed at  $T_c$  (Fig. 6.9(b)). Fig. 6.9(b) implies that the  $I_{Ag1}/I_{Si}$  ratios observed at the edges is lower than those of the corresponding bulk regions in nearly all of the samples (Inset), and an approximately linear correlation between the  $I_{Ag1}/I_{Si}$  ratio and  $d$  was obtained. The lower  $I_{Ag1}/I_{Si}$  values at the edges can be obtained from the same relationship as that in Fig. 6.9(a) (i.e., the higher peak value of  $I_{Si}$ ). Indeed, the  $I_{Ag1}/I_{Si}$  values for the FMC ( $\circ$ ) and

non-FMC (x) BPNMs, including those shown in Fig. 6.9(a), follow the peak trends for the bulk regions and edges plotted in Fig. 6.9(b), respectively.

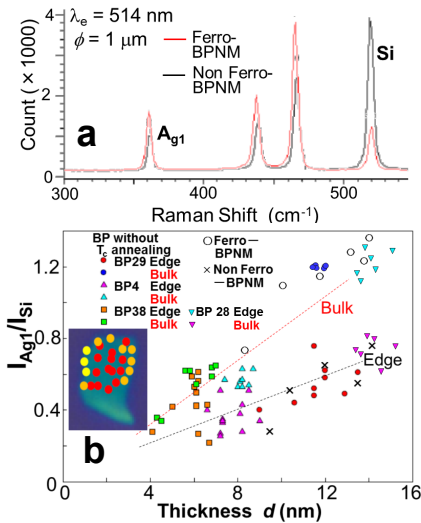


**FIGURE 6.9**

**(a)** Typical micro Raman spectra for two BPNMs that do and do not exhibit FM. **(b)** Correlation of the  $d$  and  $I_{Ag1}/I_{Si}$  values in the Raman spectra measured in the bulk and at the edges of three few-layer BP flakes (i.e., without nanopores) without  $T_c$  annealing. The linear dotted lines indicate trends for the individual correlations. The  $I_{Ag1}/I_{Si}$  values for the FM ( $\circ$ ) and non FM ( $\times$ ) BPNMs, including the result of Fig. 4(a), are also noted. **Inset:** Example of Raman mapping for sample BP4 in main panel. Red, orange, and yellow symbols mean the measured points with results of  $I_{Ag1}/I_{Si} > 0.5$ ,  $0.5 > I_{Ag1}/I_{Si} > 0.3$ ,  $0.3 > I_{Ag1}/I_{Si}$ , respectively. [65]

The lower  $I_{Ag1}/I_{Si}$  values at the edges of BP flakes can be attributed to the following two possibilities; (1) Presence of the armchair-rich edges or (2) Influence of the scattered laser beam from the Si substrate. Possibility (1) originates from the following two reasons. First, because the BP flakes without nano-pores were just mechanically exfoliated from bulk BP without any intentional alignment of crystal axis and not by annealing at the  $T_c$ , the edge atomic structures should be rough edges but arm chair rich. This is because zigzag edge appears only when crystal axis is perfectly aligned along Y axis in Fig. 6.6(a), while in any other cases the buckling armchair edge appears.

Second, the intensity of the phonons from the Si substrate at the armchair edges is higher than that of phonons at the zigzag edges, because the buckling armchair structures are formed along z-axis (Fig. 6.6(a)) and the surface of the Si substrate can easily oscillate under them (e.g., beneath gray P atoms). Indeed, the phonon dispersion along the zigzag direction was shown to be sharper than that along the armchair direction using first-principles calculations for BP [46]. However, these effects are suppressed in bulk region in few layer BPs and, hence, the  $I_{Ag1}/I_{Si}$  values are not high. On the other hand, all phonons are induced more effectively in sample edges than at bulk regions, because the sample has a free end. This inducement is more significant for phonon arising from Si substrate under the buckling arm chair structure from the abovementioned reasons.

On the other hand, possibility (2) directly results in high  $I_{Si}$ . As mentioned above, the  $I_{Ag1}/I_{Si}$  values for the FMC and non-FMC BPNMs follow the peak trends for the bulk regions and edges plotted in

Fig. 6.9(b). Because the pore structures (i.e., diameter and hexagonal shape) observed by SEM and atomic-force microscope are almost the same in these two-type BPNMs, contribution of the possibility (2) should be also the same. This cannot explain different  $I_{Si}$  in Fig. 6.9. Therefore, possibility (1) is the origin for Fig. 6.9.

Hence, the low  $I_{Ag1}/I_{Si}$  ratios arising from the high  $I_{Si}$  values in Fig. 6.9(a) suggest the buckling armchair-rich pore edges in the non-FMC BPNM. In contrast, it can be concluded that the pore edge of the FMC BPNMs is zigzag rich, which are formed by edge reconstruction during annealing at the  $T_c$ . This also suggests emergence of partial zigzag edges in other four pore edges in addition to the two zigzag pore edges (inset of Fig. 6.7(a)). Only two out of ten BPNMs did not result in zigzag-rich pore edges after annealing at the  $T_c$ , thus did not exhibit FM due to this armchair-rich edge. It also suggests that the buckling armchair edge requires higher energy for stability after the  $T_c$  annealing and is hard to be realized. The reconstruction by the  $T_c$  annealing may introduce relaxed structure to inter-pore BPNRs, which conventionally results in Peierls transition and disappearance of magnetism [44,47]. However, the present BPNM structure, in which six BPNRs with a typical width  $\sim 20\text{nm}$  form one hexagonal unit cell leaving a nano pore at the center, may prevent occurrence of Peierls transition.

### Theoretical analysis

To theoretically reconfirm the present edge-magnetism in O-ZPNRs, Soriano *et al.* have carried out first principles calculations. Figure 6.10(a) shows the band structure of the relaxed O-terminated 10-ZPNRs (Fig. 6.10(b)) considered in our calculations. The left and right panels correspond to the spin-unpolarized and -polarized cases, respectively. Similarly to previous calculations, a pair of midgap states (red arrow in Fig. 6.10(a)) span across the band gap and cross the Fermi level at around  $\pi/2a$  of the Brillouin zone (BZ) inducing a metallic state. The midgap states at  $\Gamma$  and X (right panel of Fig. 6.10(a)) are completely localized along the edges as seen in Figs. 6.10(b) and 6.10(c). This is related to the small band splitting observed at the  $\Gamma$ -point for O-terminated PNRs, which is much smaller than [50], and implies a strong reduction of inter-edge coupling in presence of O. This is in agreement with Fig. 6.8(a).

We have also checked inter-edge magnetic coupling for both parallel and antiparallel couplings of edge-FMC and edge-Anti-FMC (AFMC) configurations in the doubly relaxed unit cells. We found that the total energies were very similar ( $\Delta E < 1\text{ meV}$ ), which highlights the small spin interaction between edges. The edge-FMC configuration with antiparallel inter-edge coupling (similar to zigzag GNRs) always led to non-magnetic or bad converged solutions. In contrast, the edge-AFMC configuration always converged very fast while keeping the initial AFMC guess along the edge. Interestingly, the O atoms were not initially polarized and became magnetic during the self-consistency calculation.

The magnetic moments emerging at the O atoms couple ferromagnetically with the ones at the neighboring  $P_{edge}$  atoms giving rise to a huge enhancement of the edge magnetism (the green arrows in Fig. 6.10(c)). The values of the local magnetic moment  $M_L$  at the  $P_{edge}$  and O atoms for the O-terminated 10-ZPNR are  $|M_P| = 0.55 \mu_B$  and  $|M_O| = 0.4 \mu_B$ , respectively (very similar to the O-terminated 6-ZPNR). The calculated total  $M_L$  is around  $1 \mu_B$  per P=O dimer, almost seven times bigger than those in [47]. We also reveal that at the X-point the spin densities from the valence bands are only localized along the edges of the NR which strongly contributes to the edge-Anti-FMC state. Although the  $M_L$  value is only a few times larger than that of the FMC-GNMs ( $M_L \sim 0.2$  or  $0.3 \mu_B$ ), the uniform oxidation of pore edges through all layers in a BPNM allows this large magnetism. Since the H-termination eliminates the abovementioned unsaturated bond, magnetism disappears.

Interlayer edge-spin coupling in the O-ZPNRs also strongly contributes to the FM as shown in Figs. 6.10(c) and 6.10(d). Misalignment of interlayer adjacent O=P<sub>edge</sub> atoms in AB stacking allows FMC spin configuration in bilayer ZPNRs (Fig. 6.10(c)) as well as the case of few-layer GNRs. However, the strong interlayer interaction due to the O atom induces this FMC spin alignment and makes spin ordering more stable. Indeed, the linear scaling of the absolute magnetization, defined as the sum of the absolute values of the M<sub>i</sub> ( $m_i$ ) on each atom,  $|M| = \sum_i |m_i|$ , is confirmed with the number of layers ( $N$ ) as shown in Fig. 6.10(d). This is qualitatively consistent with Fig. 6.8(b).

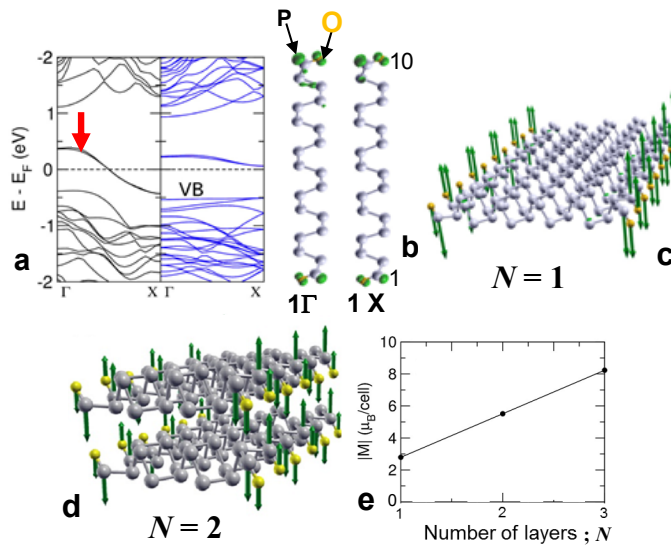


**FIGURE 6.10**

(a) Band structures for O-terminated 10-ZPNR. Left and right panels correspond to spin-unpolarized and -polarized cases. (b) Charge density contribution (shown in green) of one of the midgap states (red arrow in (a)) at  $\Gamma$  and X. The structure corresponds to O-terminated inter-pore ZPNR region of BPNM. Distances are very similar to those reported for mono-layer PNR. The distance between P and O atoms at the edges is 1.5 Å, which corresponds to a P=O double bond. (c, d) Illustration of the edge anti-FM emerging at (c) the mono-layer zigzag edges corresponding to (b) and (d) the bi-layers. Green arrows correspond to the spin magnetic moment computed on each atom. (e) Scaling of the absolute magnetization per unit cell with number of layers ( $N$ ). Relaxed interlayer-distance ( $d_z \approx 0.198$  nm) is around 0.1 nm shorter than previously report. [calculated by D. Soriano and S. Roche, ref. (65)]

In conclusion, a room-temperature large edge FM in O-BPNMs that is  $\sim 100$  times/area larger than that reported for FGNMs has been described. In contrast to H-GNMs where edge hydrogenation is hard to be completed under H<sub>2</sub> atmosphere and is not as stable, O-termination of BPNMs is robust in air atmosphere. Moreover, while O-termination suppresses magnetization in GNMs, oxidation enhances edge magnetism in BPNMs. Therefore, the emergence of magnetization with O-termination should be significantly advantageous compared to the H-termination in GNMs for the generation of edge magnetisms. This result is also the first experimental report of edge-driven magnetism in BP. Additionally, the first principles calculation has revealed that the ferromagnetic coupling of edge P atom with O atom and the strong spin localization of edge valence band can be the origins for the colossal edge magnetism observed. Moreover, interlayer interaction due to the AB stacking induces FM spin alignment and makes spin ordering stable.

## Tunneling magnetoresistance junctions realized by ferromagnetic graphene nanomesh electrode

Spintronics are highly promising issue as a key technology for next generation [51-57]. They have the following two prospects, i.e., (1) Zero-emission energy and (2) replacement of CMOS technology (i.e., beyond CMOS). From the first prospect, electron spin currents carry and emit no energy and no heat. This strong advantage resolves heat problems in large-scale integration circuits, personal computers, and also any systems loading them. In particular, heat problems become much significant in extremely closed spaces (e.g., on aerospace and air planes). Spintronic devices and circuits and systems must be extremely effective for such systems. From the second viewpoint, it is desirable subject for human life to realize devices beyond CMOS FETs, which are approaching its integration and operation limits. Although many materials and technologies have tried this, it is not yet realized. Spintronic devices based on some kinds of novel ideas must realize this. For instance, operation utilizing instant spin flipping leads to extremely high switching devices (e.g., in pico-seconds), which exceed operation speeds of CMOS FETs and LSIs. Spin quantum bits using superposition of the two quantum spin states also enable processing extremely large amount of information by parallel processing even in much smaller-scale integration compared to CMOS circuits. Therefore, spintronic devices are desired as future key technology.

Various kinds of structures have been developed for spintronics [51-57], such as giant magnetoresistance (GMR) [51], TMR [52,53], and spinvalve structures. In particular, TMR structure has realized high efficiency of TMR ratio,  $\Delta R/R_0$ , defined as  $(R_{AP}-R_P)/R_P$ , where AP and P refer to antiparallel and parallel orientations of the spin configurations (magnetizations) of the two electrodes. Even TMR ratio of as high as over 1000% has been obtained by using CoFeB/MgO/CoFeB junction.

Moreover, a variety of materials have been developed for spintronic devices, e.g., ferromagnetic metals (e.g., cobalt (Co), iron (Fe), chromium (Cr), manganese (Mn)) [55-57] and ferromagnetic semiconductors ((In, Mn), As) etc.). In contrast, in any cases, rare metals are required for the present spintronics. That is a fatal problem for the current limitation of rare material resource.

On the other hand, some theoretical works have predicted spin-based phenomena realizable without using rare-magnetic elements (i.e., graphene edges). For instance, spin-filtering (rectifying) effect predicted that GNRs with antiferromagnetic spin alignment on two edges can manipulate only electron spins with the same moment by applying in-plane electric fields [22]. Realization of (quantum) spin Hall effect (SHE) was also predicted by resolving double degeneration of edge spin bands (e.g., by introducing spin orbit interaction (SOI)) and controlling two spins with opposite moments existing in different two bands by applying electric fields [25-27]. Indeed, observation of a large spin diffusion current in high-quality graphenes fabricated on hexagonal boron-nitride (BN) and SiC substrates and also SHE in lightly hydrogenated graphenes with introducing SOI [58,59] has been experimentally confirmed. They are opening doors to novel all-carbon spintronics without using rare metals. Large spin coherence of graphenes must lead to high-efficiency spintronic devices.

Therefore, polarized edge spins and edge-driven magnetisms observed in the FGNMs and FBPNM as described in sections 1 and 2 become highly important and desirable. Also from other viewpoints, GNMs are highly expected as quantum-information [60,61], optical [62], and semiconducting-operation [63] devices. In this section, I explain an example of application how one can create spintronic devices based on the FGNM [64]. Although it is just a prototype structure, further development must bring quick and considerable advancement of this field in near future.

### TMR Junction structures consisting of the Co/SiO<sub>2</sub>/FGNM

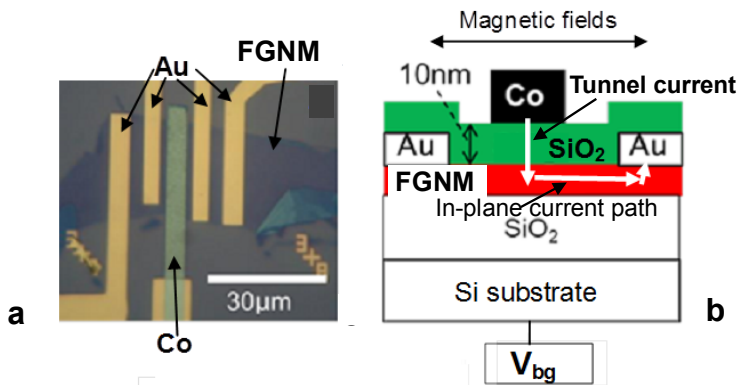


**FIGURE 6.11**

(a) Optical microscope image of a top view of the electrode pattern of the Co/SiO<sub>2</sub>/FGNM TMR junction. MR between the top Co electrode and the Au electrode located at the nearest right side was measured under constant current mode of 1 nA. (b) Schematic cross section of the TMR junction. The white line illustrates the constant current path. Thickness of the SiO<sub>2</sub> tunnel barrier of ~10 nm was confirmed by ellipsometry. Magnetic fields were applied in parallel with the FGNP plane. A back gate voltage ( $V_{bg}$ ) was applied from the back side of the Si substrate via surface SiO<sub>2</sub> film of Si substrate. [64]

TMR junctions utilizing such FGNMs as ferromagnetic electrodes are realized for the first time. The fabricated TMR junction consists of Co/SiO<sub>2</sub>/FGNM (Figs. 6.11(c) and 6.11(d)), serving as a prototype structure for rare-metal free graphene-based TMR. The honeycomb-like array of hexagonal nanopores forming the FGNM is shown in the atomic force microscope image (Fig. 6.11(a)) and in a schematic view (Fig. 6.11(b)). Fabrication followed our previous non-lithographic method, which realized the low defects and low contamination of the zigzag pore edges.

The fabricated TMR structure using this FGNM as one-side electrode with the optical microscope is shown in Fig. 6.11(a) (top-view), and is schematically described in Fig. 6.11(b). The TMR behavior is measured along the constant current path illustrated in Fig. 6.11(b). The TMR ratio is defined as the difference between the resistance values ( $R_B$ ) at individual magnetic fields ( $B$ ) and the minimum MR value ( $R_{min}$ ), which is assumed to be the best parallel spin alignment between Co electrode and FGNM; i.e., TMR ratio =  $(R_B - R_{min})/R_{min}$ . A magnetization measurement of the overlayered structure of the SiO<sub>2</sub>/FGNM implies the persistence of the ferromagnetic signal even after evaporation of the SiO<sub>2</sub> film on the pore edges, although the magnitude is reduced somewhat compared with that without SiO<sub>2</sub> film.

### TMR properties of the Co/SiO<sub>2</sub>/FGNM junction

Figure 6.12a and 6.12b give the result of a typical TMR measurement of the Co/SiO<sub>2</sub>/FGNM junction (shown in Fig. 6.11) under in-plane parallel  $B$  at (a) 1.5K and (b) 300K. The minimum resistance ( $R_{min}$ ) is identified as the situation in which the external  $B$  induces best matching between the spin polarizations of the magnetic materials (i.e., parallel spin alignment between cobalt and FGNM) and take this as  $R_p$  in subsequent calculations of TMR ratios, as mentioned in the figure caption. The observed TMR behaviors in Fig. 6.12(a) are significantly different from those of any other conventional TMR junctions. They exhibit the following unique  $B$ -dependent characteristics. (1)

TMR ratio is tuned by the  $B$  and can reach a signal about 20%. (2) The minimum of TMR ratio appears as  $B$  approaches to zero in  $-B$  region. (3) The TMR ratios increases gradually crossing  $B = 0$ . (4) The peak of TMR ratio emerges in  $+B$  region. A similar behavior is observed for polarity changes in  $B$ , i.e., when sweeping from  $+B$  to  $-B$ , (the black line in Fig. 6.12). As illustrated in the curves around zero-TMR ratio, the Co/SiO<sub>2</sub>/bulk graphene junction (i.e., without the nanopores) shows drastically different behavior, with showing unclear TMR signatures. This suggests that the TMR-like behavior observed in the Co/SiO<sub>2</sub>/FGNM junction is unique to the present TMR structure, and is driven by spin tunneling properties between the Co electrode and the FGNM. Present reproducibility of the TMR behaviors is over 80%, because six of seven samples showed similar behaviors to date.

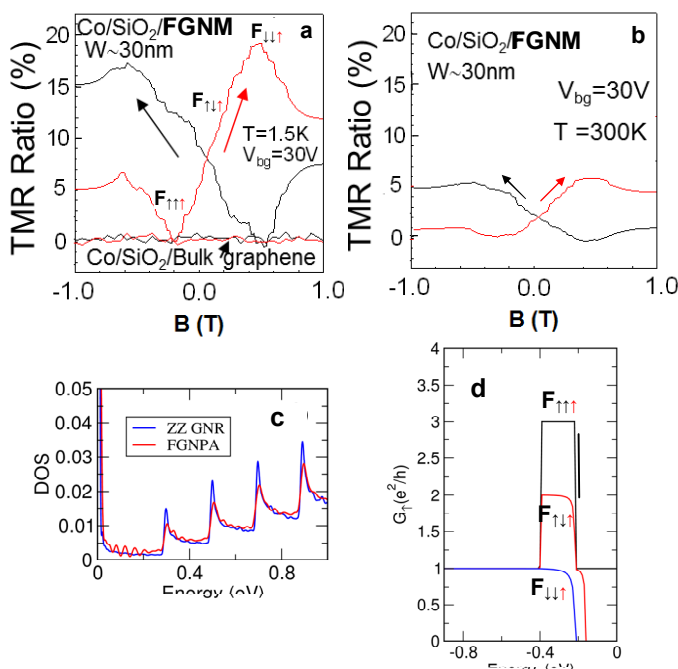


**FIGURE 6.12**

Typical TMR measurement results of the Co/SiO<sub>2</sub>/FGNM junction (shown in Fig. 6.11) under in-plane parallel  $B$  at (a) 1.5K and (b) 300K. In-plane  $B$  sweeps were performed from  $B = -1$  to  $+1\text{ T}$  (red line) and  $B = +1$  to  $-1\text{ T}$  (black line). Mostly constant zero TMR ratios shown in (a) are TMR values for the bulk graphene/SiO<sub>2</sub>/Co junction. Notation  $F_{\uparrow\uparrow\uparrow}$  means spin configuration of the two edges of an interpore GNR region in the FGNMs (left two black-arrows) and the Co (right one red-arrow). (c) Density of states calculated for the GNM with an interpore distance of  $W \sim 10\text{ nm}$  and a pore diameter of  $\sim 80\text{ nm}$  and the related zigzag GNR. (d) Conductance between zigzag GNR junctions with different edge spin polarization states and cobalt electrode. Note the distinct differences in the MR signal in the energy regime where edge states dominate the electronic properties of the GNR. [calculated by D. Soriano and S. Roche, ref. (64)]

TMR properties observed at room temperature are shown in Fig. 6.12(b). Maximum TMR ratios decreases from  $\sim 20\%$  to  $\sim 5\%$  owing to the reduced flat-band FM and the behaviors become much ambiguous compared with those at low temperatures, showing non-zero TMR ratios at high  $B$  due to thermal spin instability. It should be noticed that, nevertheless, TMR behaviors are still observable.

The observed unique TMR behavior can be qualitatively understood by considering the spin alignment between two opposing pore edges of the FGNM (i.e., two edges of the interpore GNR region) and the Co electrode. It also clarifies spin ground states of the H-terminated zigzag-type GNRs under no  $B$ . We support these interpretations by atomistic simulations. First, we calculate the density of states (DOS) of a GNM reminiscent of the fabricated structure. The calculated DOS (Fig. 6.12(c)) is compared to that obtained for an infinitely long zigzag GNR (i.e., interpore GNR region). Ignoring the tunnel barrier, the TMR device is thus conveniently visualized as a junction between a Co spin injector and an array of uncoupled zigzag GNRs, the spin polarizations of which depend on the  $B$ . Based on this result, it is simulated the spin transport properties of the device via a zigzag GNR-based junction, in which the spin polarization is differentiated between left (Co spin injector) and right (FGNM) parts (Fig. 6.13(d)). The sweep from  $-B$  to  $+B$  (red curve in Fig. 6.12(a)) is focused. As indicated in Fig. 6.12(d), three distinct regions are identified in the TMR response, corresponding to the situations where the magnetization of the FGNM (i.e., spin alignment of two edges of the interpore GNRs) is ferromagnetic ( $F_{\uparrow\uparrow}$ ; the two black arrows at the subscript mean the spin moment of two edges of the interpore GNR) with spins parallel to the spin injector (Co) ( $F_{\uparrow\uparrow\uparrow}$ ; the red subscript arrow is the spin moment of injector), anti-ferromagnetic (AF;  $F_{\uparrow\downarrow\uparrow}$ ), and ferromagnetic with spins anti-parallel to the spin injector ( $F_{\downarrow\downarrow\uparrow}$ ). At  $-B$ , the spins of the injector and the FGNPA are largely parallel ( $F_{\uparrow\uparrow\uparrow}$ ), resulting in maximum conductance through the junction (Fig. 6.12(d)), and thus the minimum of the TMR ratio in Fig. 6.12(a). As the  $B$  approaches zero, the GNR array (i.e., ensemble of the two edges of the interpore GNRs) gradually transitions to an AF configuration ( $F_{\uparrow\downarrow}$ ), where half of the conductance channels are suppressed, resulting in the half value of conductance (Fig. 6.12(d)) and gradual increase in the TMR ratio ( $F_{\uparrow\downarrow\uparrow}$ ). As the  $B$  is increased further to  $+B$ , the spin polarization of the GNR array changes to the ( $F_{\downarrow\downarrow}$ ) configuration, suppressing all edge conductance channels, resulting in the conductance minimum (Fig. 6.12(d)) and subsequent the peak of TMR ratio observed around  $B = 0.5$  T ( $F_{\downarrow\downarrow\uparrow}$ ). These calculation suggests that gradual changes in TMR ratios can be actually possible. At higher  $+B$ , the spins of the Co injector start to align with the magnetic field, gradually quenching the TMR ratio, while non-zero TMR ratios in higher  $+B$  regions suggest instability of the pore edge spins of the FGNMs as well as those in  $-B$  region .

It implies that the edge polarized spins of the interpore GNR regions can actually tunnel through  $\text{SiO}_2$  barrier forming the spin alignment with the spins of Co electrode and also that the spin ground states of the H-terminated zigzag-GNRs are AF under no  $B$ . This result is consistent with our previous experimental results, which exhibited ferromagnetism only when  $B$  is applied. It is important to note that the main mechanism revealed by the present simulations does not depend on how the electrons are really injected from the cobalt electrode to the GNM, but how efficiently spin-polarized electrons injected on the GNM are further transmitted depending on the magnetic ordering of the local moments along the zigzag edges.

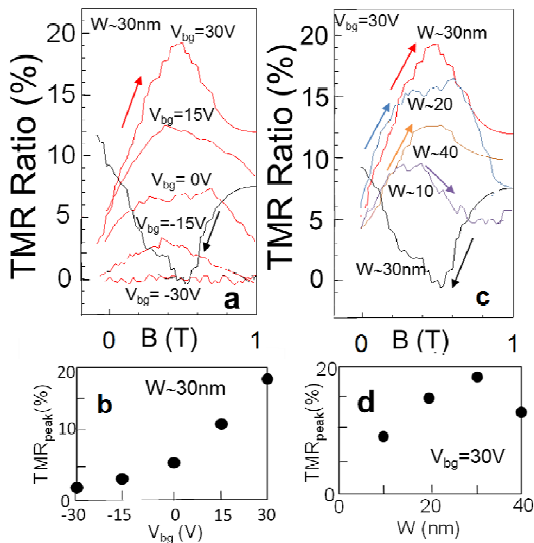


**FIGURE 6.13**

(a) Measurements of the sample shown in Fig. 6.12 for  $V_{bg}$  from +30 V to -30 V are shown by red curves, while a black line shows that for  $-B$  to  $+B$  regions for reference. (b)  $V_{bg}$  dependence of peak values of the TMR ratios shown in Fig. 6.13(a). (c) Measurements of a sample similar to that in Fig. 6.12(a) but with different  $W$ . Exhibited  $B$  regions are the same as Fig. 6.13(a). (d)  $W$  dependence of peak values of the TMR ratios shown in Fig. 6.13(c). [64]

Here, the TMR characteristics can be also controlled by changing a back gate voltage ( $V_{bg}$ : Fig. 6.11(d)) (Figs. 6.13(a) and 6.13(b)), as well as to the interpore spacing ( $W$ ; i.e., width of interpore GNRs) (Figs. 6.13(c) and 6.13(d)). The TMR ratio exhibits a maximum value of  $\sim 20\%$  at  $V_{bg} = +30\text{V}$  (Figs. 6.13(a), and 6.13(b)), while it is reduced with decreasing  $V_{bg}$  toward  $-V_{bg}$  region. This is consistent with the presence of evident spin-based phenomena observed only at  $V_{bg} = +30\text{V}$  for previous in-plane MR behaviors of FGNM. This is because the Au electrode was placed at the side position of the Co/SiO<sub>2</sub>/FGNM junction and the in-plane spin current path exists through the H-terminated FGNM between the TMR junction and the Au electrode in the present specified sample structure (Fig. 6.11(d)). Although the polarized spins at the pore edges and TMR ratio themselves have basically no correlation with the  $V_g$ , the spin current through the in-plane path is significantly reduced with decreasing  $V_g$  due to the n-type semiconducting behavior of the interpore GNR regions of the GNM. This makes TMR features difficult to detect, resulting in the decreases in the observed TMR ratios.

For larger interpore spacing of  $W \sim 40\text{ nm}$ , the TMR value further decreases significantly (Figs. 6.13(c) and 6.13(d)). For such a large spacing, the spin polarization of opposing pore edges (i.e., two edges of interpore GNRs) becomes unstable due to suppressed spin interaction, quenching the TMR properties. TMR ratios also decrease when using FGNM with smaller  $W$  (Figs. 6.13(c) and 6.13(d)), because  $W \leq 20\text{ nm}$  is too narrow to form spin currents along the in-plane current path through the FGNM to Au electrode (Fig. 6.11(d)). Although FM is stronger for smaller  $W$ , induced scattering by the nanopore array heavily obstructs spin flow to the Au electrode, reducing the TMR ratio. This is again consistent with previously observed spin-based phenomena in FGNM with  $W \sim 30\text{ nm}$ . Therefore, the optimum  $W$  value exists for the TMR ratios.

### TMR properties of annealed junctions

The unique TMR behaviors in the Co/SiO<sub>2</sub>/FGNM junctions have been presented. Nevertheless, the maximum TMR ratio is as low as ~20% at best (Fig. 6.12(a)). One of the main reasons is the poor interaction at the lattice-mismatched SiO<sub>2</sub>/FGNM interface, particularly at the H-terminated pore edges, which destructs transport of the spin-alignment current and reduces TMR ratios. In contrast, as shown in Fig. 6.14(a), we find that annealing of the SiO<sub>2</sub>/FGNM structure at ~500 °C right after the deposition of SiO<sub>2</sub> tunneling layer drastically (i.e., >~5 times) improves the TMR ratios of Fig. 6.12(a), although some instability of the pore edge spins still remain as some irregular small TMR ratio peaks. At room temperature, the maximum TMR ratio increases even by ~10 times (Fig. 6.14(b)) compared to that in Fig. 6.12(b).

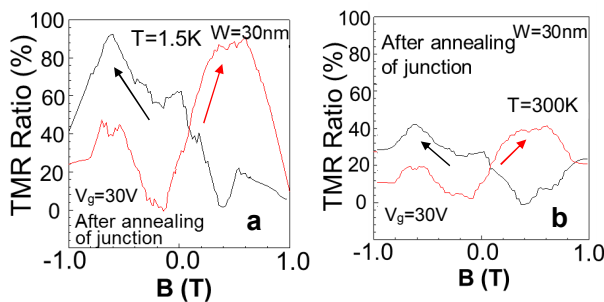


**FIGURE 6.14**

TMR behaviors of the Co/SiO<sub>2</sub>/FGNM junction improved by annealing, at (a) 1.5K and (b) 300K. The annealing of SiO<sub>2</sub>/FGNPA junction at 500 °C was carried out under high vacuum atmosphere right after depositing of SiO<sub>2</sub> layer on FGNM. [64]

This promises that introducing a lattice-matched tunnel barrier layer (e.g., graphene oxide) instead of SiO<sub>2</sub> layer and also improvement of magnitude of the ferromagnetism in the FGNMs (e.g., utilizing HSQ resist treatment) can increase TMR ratios further and make evident room-temperature operation possible. Moreover, realization of FGNM/(lattice-matched tunnel barrier)/FGNM junction must significantly improve the performance of the TMR behaviors toward ~1000 % order.

## Conclusion

The room-temperature edge-driven FMs arising from the flat energy band in zigzag H-GNMs and from the ferromagnetic spin coupling edge O=P bonds in few-layer zigzag O-BPNMs and the application of the ferromagnetic H-GNM to TMR devices have been presented. Because easy full-oxidation of the pore edges only by exposing BPNMs into air atmosphere leads to a large-amplitude FM, it will quickly realize magnetic and spintronic devices in near future. Very recently, room-temperature FMs in O-terminated few-layer hexagonal boron-nitride has been also found [66]. The formation and the control of a room temperature magnetic order in 2D atom-thin materials can be actually major milestones for the advent of innovative magnetic- and spintronic-based technologies. Further advancement of the room-temperature FM realized in these NM structures

on 2D atom-thin layers is highly valuable for the context of flexible and wearable atomic strategies and spintronics for which FM is required without using rare (-earth) magnetic atoms.

## Acknowledgments

The author thanks D. Soriano, S. Roche, H. Yang, M. Chshiev, J. Akimitsu, K. Horigane, T. Muranaka, T. Nakamura, K. Fujita, Y. Hashimoto, Y. Iye, S. Katsumoto, M. Yamamoto, S. Tarucha, H. Hibino, T. Ando, T. Enoki, Y. Yagi, A. H. Macdonald, P. Seneor, R. Wiesendanger, M. S. Dresselhaus and my students and staff for their technical contribution, fruitful discussions, and encouragement. This work was partly supported by a Grant-in-aid for Scientific Research (15K13277, 24241046) in MEXT, a High-Technology Research Center Project for private universities in MEXT, and Air-Force of Scientific Research grant at USA.

## References

1. Nakada, K., Fujita, M., Dresselhaus, G., Dresselhaus, M.S. "Edge state in graphene ribbons: Nanometer size effect and edge shape depend". *Phys. Rev. B*, (1996) **54**, 17954.
2. Fujita, M., Wakabayashi, K., Nakada, K., Kusakabe, K. "Peculiar localized state at zigzag graphite edge". *J. Phys. Soc. Jpn.*, (1996) **65**, 1920 – 1923.
3. Kusakabe, K., Maruyama, M. "Magnetic nanographite". *Phys. Rev. B*, (2003) **67**, 092406.
4. Okada, S., Oshiyama, A. "Magnetic Ordering in Hexagonally Bonded Sheets with First-Row Elements". *Phys. Rev. Lett.*, (2001) **87**, 146803.
5. Lee, H., Son, Y., Park, N., Han, S., Yu, J. "Magnetic ordering at the edges of graphitic fragments: Magnetic tail interactions between the edge-localized states". *Phys. Rev. B*, (2005) **72**, 174431.
6. Veiga, R.G.A., Miwa, R.H., Srivastava, G.P. "Quenching of local magnetic moment in oxygen adsorbed graphene nanoribbons". *J. Chem. Phys.*, (2008) **128**, 201101.
7. Lee, H., Park, N., Son, Y., Han, S., Yu, J. "Ferromagnetism at the edges of the stacked graphitic fragments: An *ab initio* study". *Chem. Phys. Lett.*, (2004) **398**, 207–211.
8. Asano, H., Muraki, S., Endo, H., Bandow, S., Iijima, S. "Strong magnetism observed in carbon nanoparticles produced by the laser vaporization of a carbon pellet in hydrogen-containing Ar balance gas". *J. Phys.*, (2010) **22**, 334209.
9. Enoki, T. and Takai, K. "The edge state of nanographene and the magnetism of the edge-statespins". *Sol. Stat. Comm.*, (2009) **149**, 1144–1150.
10. Niimi, Y., Matsui, T., Kambara, H., Tagami, K., Tsukada, M., Fukuyama, H. "Scanning tunneling microscopy and spectroscopy of the electronic local density of states of graphite surfaces near monoatomic step edges". *Phys. Rev. B*, (2006) **73**, 085421.
11. Son, Y.W., Cohen, M.L., Louie, S.G. "Energy gaps in graphene nanoribbons". *Phys. Rev. Lett.*, (2006) **97**, 216803.
12. Yang, L., Park, C., Son, Y., Cohen, M.L., Louie, S.G. "Quasiparticle energies and band gaps in graphene nanoribbons". *Phys. Rev. Lett.*, (2007) **99**, 186801.
13. Shima, N. and Aoki, H. "Electronic structure of super-honeycomb systems: A peculiar realization of semimetal/semiconductor classes and ferromagnetism". *Phys. Rev. Lett.*, (1993) **71**, 4389–4392.

14. Rosser, J.F., Palacios, J.J. "Magnetism in Graphene Nanoislands". *Phys. Rev. Lett.*, (2007) **99**, 177204.
15. Jia, X., Hofmann, M., Meunier, V., Sumpter, B.G., Campos-Delgado, J.; Romo-Herrera, J.M.; Son, H.; Hsieh, Y.; Reina, A.; Kong, J. "Controlled formation of sharp zigzag and armchair edges in graphitic nanoribbons". *Science*, (2009) **323**, 1701–1705.
16. Girit, Ç.Ö., Meyer, J.C., Erni, R., Rossell, M.D., Kisielowski, C., Yang, L., Park, C., Crommie, M.F., Cohen, M.L., Louie, S.G. "Graphene at the edge: Stability and dynamics". *Science*, (2009) **323**, 1705–1708.
17. Shimizu, T., Haruyama, J., Marcano, D.C., Kosinkin, D.V., Tour, J.M., Hirose, K., Suenaga, K. "Large intrinsic energy bandgaps in annealed nanotube-derived graphene nanoribbons". *Nat. Nanotech.*, (2011) **6**, 45–50.
18. Han, M.Y., Brant, J.C., Kim, P. "Electron transport in disordered graphene nanoribbons". *Phys. Rev. Lett.*, (2010) **104**, 056801.
19. Wang, X., Ouyang, Y., Li, X., Wang, H., Guo, J., Dai, H. "Room-temperature all-semiconducting sub-10-nm graphene nanoribbon field-effect transistors". *Phys. Rev. Lett.*, (2008) **100**, 206803.
20. Krauss, B., Nemes-Incze, P., Skakalova, V., Biro, L.P., von Klitzing, K., Smet, J.H. "Raman scattering at pure graphene zigzag edges". *Nano Lett.*, (2010) **10**, 4544–4548.
21. Bai, J., Zhong, X., Jiang, S., Huang, Y., Duan, X. "Graphene nanomesh". *Nat. Nanotech.*, (2010) **5**, 190–194.
22. Son, Y.W., Cohen, M.L., Louie, S.G. "Half-metallic graphene nanoribbons". *Nature*, (2006) **444**, 347–349.
23. Takesue, I., Haruyama, J., Kobayashi, N., Chiashi, S., Maruyama, S., Sugai, T., Shinohara, H. "Superconductivity in entirely end-bonded multiwalled carbon nanotubes". *Phys. Rev. Lett.*, (2006) **96**, 057001.
24. Murakami, S., Nagaosa, N., Zhang, S. "Dissipationless quantum spin current at room temperature". *Science*, (2003) **301**, 1348–1351.
25. Kane, C.L. and Mele, E.J. "Quantum spin Hall Effect in grapheme". *Phys. Rev. Lett.*, (2005) **95**, 226801–226804.
26. Kane, C.L. "Graphene and the quantum spin Hall Effect". *J. Mod. Phys. B*, (2007) **21**, 1155.
27. Schmidt, M.J. and Loss, D. "Edge states and enhanced spin-orbit interaction at graphene/graphane interfaces". *Phys. Rev. B*, (2010) **81**, 165439.
28. Otani, M., Koshino, M., Takagi, Y., Okada, S. "Intrinsic magnetic moment on (0001) surfaces of rhombohedral graphite". *Phys. Rev. B*, (2010) **81**, 161403 (R).
29. Yang, H., Chshiev, M., Boukhvalov, D.W., Waintal, X., Roche, S. "Inducing and optimizing magnetism in graphene nanomeshes". *Phys. Rev. B*, (2011) **84**, 214404.
30. You, Y.M., Ni, Z.H., Yu, T., Shen, Z.X. "Edge chirality determination of graphene by Raman spectroscopy". *Appl. Phys. Lett.*, (2008) **93**, 163112.
31. Soriano, D., Leconte, N., Ordejón, P., Charlier, J., Palacios, J., Roche, S. "Magnetoresistance and magnetic ordering fingerprints in hydrogenated grapheme". *Phys. Rev. Lett.*, (2011) **107**, 016602.
32. Abanin, D.A., Morozov, S.V., Ponomarenko, L.A., Gorbachev, R.V., Mayorov, A.S., Katsnelson, M.I., Watanabe, K., Taniguchi, T., Novoselov, K.S., Levitov, L.S. "Giant nonlocality near the Dirac point in grapheme". *Science*, (2011) **332**, 328–330.
33. Shimizu, T., Nakamura, J., Tada, K., Yagi, Y., Haruyama, J. "Magnetoresistance oscillations arising from edge-localized electrons in low-defect graphene antidot-lattices". *Appl. Phys. Lett.*, (2012) **100**, 023104.

34. Tada, K., Hashimoto, T., Haruyama, J., Yang, H., Chshiev, M. "Spontaneous spin polarization and spin pumping effect on edges of graphene antidot lattices". *Phys. Status Solidi*, (2012) **249**, 2491–2496.; Haruyama, J. "Graphene and Graphene NanomeshSpintronics", Special Issue on "Carbon Nanoelectronics" in *Electronics*, (2013) **2(4)**, 368-386.
35. Tada, K., Hashimoto, T., Yagi, Y., Haruyama, J., Yang, H., Chshiev, M. "Electron-Spin-Based Phenomena Arising from Pore Edges of Graphene Nanomeshes", *Journal of superconductivity and novel magnetisms*, (2013) **26**, 1037.
36. Hashimoto, T., Kamikawa, S., Yagi, Y., Haruyama, J., "Electronic Properties of Nanopore Edges of Ferromagnetic Graphene Nanomeshes at High Carrier Densities under Ionic-Liquid Gating", *Materials Sciences and Applications*, 2014, **5**, 1-9.
37. Kato, T., Nakamura, T., Haruyama, J. *et al.*, "High-Efficiency graphene nanomesh magnets realized by controlling hydrogenation of pore edges". *Appl. Phys. Lett.* 2014, **104**, 252410.
38. Lieb, E. H. "Two theorems on the Hubbard model", *Phys. Rev. Lett.* **62**, 1201-1204 (1989).
39. Li, L. *et al.*, "Black phosphorus field-effect transistors". *Nature Nanotech.* (2014) **9**, 372.
40. Herrero, P.-J. *et al.*, "Phosphorus joins the family". *Nature Nanotech.* (2014) **9**, 330.
41. Koenig, S. P. *et al.*, "Electric field effect in ultrathin black phosphorus". *Appl. Phys. Lett.* (2014) **104**, 103106.
42. Gomez, A. C. *et al.*, "Isolation and characterization of few-layer black phosphorus". *2D Materials* (2014) **1**, 025001.
43. Zhu, Z. *et al.*, "Magnetism of zigzag edge phosphorene nanoribbons". *Appl. Phys. Lett.* (2014) **105**, 113105.
44. Peng, X. *et al.*, "Edge effects on the electronic properties of phosphorene nanoribbons". *J. Appl. Phys.* (2014) **116**, 144301.
45. Carvalho, A., Rodin, A. S., and Neto, A. H. C., "Phosphorene nanoribbons". *Euro. Phys. Lett.* (2014) **108**, 47005.
46. Ong, Z. Y., Cai, Y., Zhang, G., Zhang, Y. –W., "Strong Thermal Transport Anisotropy and Strain Modulation in Single-Layer Phosphorene". arXiv: 1409.097
47. Du, Y. *et al.*, "Unexpected magnetic semiconductor behavior in zigzag phosphorene nanoribbons driven by half-filled one dimensional band". *Sci. Rep.* (2015) **5**, 8921.
48. Zhu, W. *et al.*, "Black Phosphorus Radio-Frequency Transistors". *Nano Lett.* (2015) **15**, 1883
49. Dai, J. and Zeng, X. C., "Bilayer phosphorene: effect of stacking order on bandgap and its potential applications in thin-film solar cells". *J. Phys. Chem. Lett.* (2014) **5** 1289-1293.
50. Luo, X., Lu, X., *et al.*, "Large Frequency Change with Thickness in Interlayer Breathing Mode—Significant Interlayer Interactions in Few Layer Black Phosphorus". *Nano Letters* (2015) **15** 3931-3938.
51. Baibich, M.N., Broto, J.M., Fert, A., Van Dau, F.N., Petroff, F.; Etienne, P.; Creuzet, G.; Friederich, A.; Chazelas, J. "Giant magnetoresistance of (001)Fe/(001)Cr magnetic superlattices". *Phys. Rev. Lett.*, (1988) **61**, 2472.
52. Moodera, J.S., Kinder, L.R., Wong, T.M., Meservey, R. "Large magnetoresistance at room temperature in ferromagnetic thin film tunnel junctions". *Phys. Rev. Lett.*, (1995) **74**, 3273–3276.
53. Yuasa, S., Nagahama, T., Fukushima, A., Suzuki, Y., Ando, K. "Giant room-temperature magnetoresistance in single-crystal Fe/MgO/Fe magnetic tunnel junctions". *Nat. Mat.*, (2004) **3**, 868–871.

54. Hayakawa, J., Ikeda, S., Lee, Y.M., Matsukura, F., Ohno, H. "Effect of high annealing temperature on giant tunnel magnetoresistance ratio of magnetic tunnel junctions". *Appl. Phys. Lett.* (2006) **89**, 232510.
55. MuneKata, H., Ohno, H., von Molnar, S., Segmüller, A., Chang, L.L., Esaki, L. "Diluted magnetic III-V semiconductors", *Phys. Rev. Lett.*, (1989) **63**, 1849–1852.
56. Ohno, H., MuneKata, H., Penney, T., von Molnár, S., Chang, L.L. "Magnetotransport properties of *p*-type (In,Mn) As diluted magnetic III-V semiconductors". *Phys. Rev. Lett.*, (1992) **68**, 2664–2667.
57. Hai, P.N., Ohya, S., Tanaka, M., Barnes, S.E., Maekawa, S. "Electromotive force and huge magnetoresistance in magnetic tunnel junctions". *Nature*, (2009) **458**, 489–492.
58. Castro Neto A. H. & Luinea, G. F. "Impurity-Induced Spin-Orbit Coupling in Graphene". *Phys. Rev. Lett.* (2009) **103**, 026804.
59. Balakrishnan, J., Koon, G. K. W., Jaiswal, M, Castro Neto, A. H. & Özyilmaz, B. "Colossal enhancement of spin-orbit coupling in weakly hydrogenated graphene", *Nature Physics* (2013) **9**, 284-287.
60. Trolle, M. L., Møller, U. S., and Pedersen, T. G., "Large and stable band gaps in spin-polarized graphene antidot lattices". *Phys. Rev. B* (2013) **88**, 195418.
61. Pedersen, T. G. et al., "Graphene Antidot Lattices: Designed Defects and Spin Qubits". *Phys. Rev. Lett.* (2008) **100**, 136804.
62. Pedersen, T. G. et al., "Optical properties of graphene antidot lattices". *Phys. Rev. B* (2008) **77**, 245431.
63. Fürst, J. A. et al., "Electronic properties of graphene antidot lattices". *New Journal of Physics* (2009) **11**, 095020.
64. Hashimoto, T., Haruyama, J., Soriano, D., Roche, S. et al., "Tunneling magnetoresistance phenomenon utilizing graphene magnet electrode". *Appl. Phys. Lett.* (2014) **105**, 183111.
65. Nakanishi, T., Haruyama, J., Soriano, D., Roche, S. et al., "Large edge-magnetism in oxidized few-layer black phosphorus nanomeshes". *Nano Research* (2016) In press
66. Ohata, C., Haruyama, J. et al., "Hexagonal boron-nitride nanomesh magnets". *Appl. Phys. Lett.* (2016) In press.